

Article

# The Corrosion Resistance of Aluminum Alloy Modified by Laser Radiation

K.M. Mroczkowska <sup>1,\*</sup> , A.J. Antończak <sup>1</sup> and J. Gąsiorek <sup>2</sup>

<sup>1</sup> Laser Micro-Processing Group; Faculty of Electronics, Wrocław University of Science and Technology, Wyb. Wyspiańskiego 27, 50-320 Wrocław, Poland; arkadiusz.antonczak@pwr.edu.pl

<sup>2</sup> Faculty of Mechanical Engineering, Wrocław University of Science and Technology, Wyb. Wyspiańskiego 27, 50-320 Wrocław, Poland; jolanta.gasiorek@pwr.edu.pl

\* Correspondence: katarzyna.mroczkowska@pwr.edu.pl; Tel.: +48-713204698

Received: 6 September 2019; Accepted: 14 October 2019; Published: 16 October 2019



**Abstract:** This study presents an analysis of the impact of the oxide layers, prepared utilizing fiber laser radiation (1062 nm) in ambient air with different process parameters, on the corrosion resistance of EN 5754 aluminum alloy. Due to both high corrosion resistance and high fatigue strength, a 5754 alloy is used, among others, in the marine, aerospace, automotive, and chemical industries. Nevertheless, it corrodes in aggressive environments (with high chloride ions concentration). The controlled delivery of laser radiation energy in the oxygen environment allows the formation of the oxide layer on the surface of the material. We have determined that it significantly affects the resistance of these materials to corrosion. As a result of laser irradiation, changes in the chemical structure of the surface layer (chemical composition as well as surface development) can be observed. It may exert both a positive and a negative consequence on the corrosion resistance. The electrochemical corrosion tests (potentiodynamic polarization and electrochemical impedance spectroscopy EIS) have been carried out in an aggressive environment (3% NaCl). Moreover, microscopic examination, chemical tests, and roughness were also performed. The study revealed that appropriate control of the laser process can significantly increase the original corrosion resistance of the 5754 aluminum alloy.

**Keywords:** laser; aluminium; NaCl; electrochemical impedance spectroscopy; scanning electron microscope; roughness

## 1. Introduction

Aluminum alloy 5754 is an important material in the industry due to its many excellent characteristics including its good corrosion resistance, proper mechanical properties (tensile strength  $R_m \sim 190\text{--}200$  MPa, modulus of elasticity  $E \sim 70$  GPa, modulus of transverse elasticity  $G = 26.5$  GPa), and low density ( $2.68$  g/cm<sup>3</sup>). The high corrosion resistance of the aluminum alloy is attributed to a thin but very tight and tightly adhering layer of aluminum oxide formed on the surface of the material. This oxide layer protects the material against further oxidation. Thanks to high corrosion resistance, it is commonly used in the marine, shipbuilding, food and chemical industries, in the production of household appliances, architecture, and the automotive industry [1]. However, despite these attractive properties, in the presence of aggressive ions, like chloride and halide, the protective layer can be locally destroyed, and a corrosive attack takes place [2].

Corrosion is a slow, progressive, or rapid deterioration of a metal's properties under the influence of the surrounding environment [3]. The main corrosion problem associated with aluminum and its alloys concerns the localized breakdown of the passive film, which leads to the initiation and growth of corrosion pits in a chloride medium [4]. The fundamental reactions of the corrosion of aluminum in an aqueous medium have been the subject of many studies [5,6]. The corrosion

resistance of Al alloys depends on many factors such as environmental, alloy composition, and microstructure factors. The fundamental reactions of the corrosion of aluminum is a result of oxidation at the anode:  $(2\text{Al} \rightarrow 2\text{Al}^{3+} + 6\text{e}^-)$  and reduction at the cathode (outside the cavity of water:  $\frac{3}{2}\text{O}_2 + 3\text{H}_2\text{O} + 6\text{e}^- \rightarrow 6\text{OH}^-$  or of  $\text{H}^+$ :  $6\text{H}^+ + 6\text{e}^- \rightarrow 3\text{H}_2$ ) [7]. Aluminum corrosion results in the formation of alumina  $\text{Al}(\text{OH})_3$ , which is insoluble in water and precipitates as a white gel. The overall reaction of pitting corrosion on aluminum is:  $2\text{Al} + 3\text{H}_2\text{O} + \frac{3}{2}\text{O}_2 \rightarrow 2\text{Al}(\text{OH})_3$ .

Past studies have shown that laser radiation can contribute to the improvement of corrosion resistance of aluminum alloy in the NaCl solution. The immersion tests, conducted by Chan et al. [8], have shown that, after KrF excimer laser treatment ( $\lambda = 248 \text{ nm}$ ,  $\tau = 25 \text{ ns}$ ), on the surface of the material, significantly fewer corrosion pits are observed when compared to the untreated specimen. Increased corrosion resistance was assigned both to the reduction of constituent particles in the laser re-melted layer and the creation of a continuous passivation layer. Additionally, the fatigue resistance in 3.5% NaCl was higher than for the reference sample. Embuka et al. [9] evaluated corrosion resistance after KrF Laser Surface Melting LSM ( $\lambda = 248 \text{ nm}$ ,  $\tau = 13 \text{ ns}$ ) using anodic polarization and immersion testing. LSM contributes to the decrease of corrosion current density and, thus, to increase the corrosion resistance of aluminum alloy when compared to the reference sample. The cross-sectional SEM analysis revealed the occurrence of pitting and intergranular corrosion on the reference sample. However, these changes were not observed on the laser-treated sample. Laser modification using a 2 kW  $\text{CO}_2$  laser ( $\lambda = 10.6 \mu\text{m}$ , CW) caused an increase of breakdown potential when compared to the untreated sample [10]. It was also confirmed that the ruby ( $\lambda = 694.3 \text{ nm}$ ,  $\tau = 15 \text{ ns}$ ) [11], Nd:YVO<sub>4</sub> ( $\lambda = 1064 \text{ nm}$ ,  $\tau = 10 \text{ ps}$ ) [12], and fiber laser ( $\lambda = 1064 \text{ nm}$ ,  $\tau = 10 \text{ ns}$ ) improves the corrosion resistance of the aluminum alloy when compared to the untreated reference sample [13]. The increase in corrosion resistance may result from the physicochemical changes in the surface layer—the  $\text{MgAl}_2\text{O}_4$  as a result of the interaction of laser radiation transforms into a new, more protective oxide layer containing  $\text{Al}_2\text{O}_3$  [13].

In the vast majority of studies (excluding the  $\text{CO}_2$  case), lasers with a short pulse duration (10 ps–25 ns) were used. In addition, only one work has been presented until now, in which a fiber laser source has been used, but, due to the main purpose of this work known as laser cleaning, research concerns a different range of process parameters [13]. The main objective of this study was to examine the corrosion resistance of the aluminum alloy after surface treatment using the commonly-used  $\text{Yb}^{3+}$ : glass long pulse duration (230 ns) fiber laser. Aluminum exerts a different absorption for this wavelength. The use of a long pulse duration fiber laser results in quite different mechanisms acting on the material. In this case, the laser acts as a heat source, creating an oxide layer, which, in some range of process parameters, can improve the corrosion resistance.

## 2. Materials and Methods

### 2.1. Substrates and Sample Preparation

The study was conducted on the 5754 aluminum alloy (2B cold rolled sheet). The chemical composition of the tested sample is listed in Table 1.

**Table 1.** Chemical composition (wt.%) of 5754 aluminum alloy.

Si	Fe	Cu	Mn	Mg	Cr	Zn	Ti	Al
0.4 <sub>max</sub>	0.4 <sub>min</sub>	0.1 <sub>max</sub>	0.5 <sub>max</sub>	2.6–3.6	0.1–0.3	0.2 <sub>max</sub>	0.15 <sub>max</sub>	residual

The plates were pre-coated with anti-scratch, polymer foil, which was removed before the experiment. Prior to corrosion tests, specimens with a dimension of  $25 \times 25 \times 1 \text{ mm}^3$ , were washed in isopropyl alcohol in an ultrasonic bath and dried with compressed nitrogen.

## 2.2. Laser Treatment

Experiments were performed using a Yb<sup>3+</sup>: glass fiber laser ( $\lambda = 1062$  nm,  $P_{\max} = 20$  W,  $\tau = 230$  ns). The laser system was equipped with a galvanometer-based optical scanner. The laser beam was focused on the target through a 160-mm focal length F-Theta lens (LINOS type 4401-305-000-21). The samples were annealed in ambient air. The beam diameter  $\omega_0$  at the focal point was approximately 40  $\mu\text{m}$ . Samples were irradiated over a  $15 \times 15$  mm<sup>2</sup> surface. Selected parameters for this experiment are shown in Table 2.

**Table 2.** Set of process parameters selected for the experiment, where:  $P$ —average laser power,  $F$ —laser energy density (fluence),  $V$ —scanning speed of the sample,  $h$ —hatching distance, and  $PRR$ —pulse repetition rate.

No.	$P$ [W]	$F$ [kJ/cm <sup>2</sup> ]	$V$ [mm/s]	$h$ [ $\mu\text{m}$ ]	$PRR$ [kHz]
1	0 (REF)	0	-	-	-
2	6	2.7			
3	8	3.6			
4	10	4.5	10	10	80
5	13	5.9			
6	16	7.2			
7	20	9.0			

The maximum accumulated laser fluence  $F$  was defined as [14]:

$$F = \frac{2\sqrt{2}P}{\pi\omega_0 V} \left[ \frac{J}{\text{cm}^2} \right]. \quad (1)$$

## 2.3. Microscopic and Chemical Analysis

The morphology of the samples was accessed using an SEM Zeiss MA25 scanning electron microscope, under the pressure of  $\sim 2$  mPa with an accelerating voltage of 20 kV. The chemical analysis was performed using both the EDS (Carl Zeiss, Cambride, United Kingdom) and Raman method. The Raman spectra were recorded in the range of 0–1500 cm<sup>-1</sup> using an HR800 (Horiba Jobin Yvon, Villeneuve-d'Ascq, France) spectrometer LabRAM, and an argon ion laser COHERENT INNOVA 400 operating at 514.55 nm. Spectra were performed with 600 line/mm grating. At least six measurement points were made for each sample, and the most representative spectra were analyzed. The base line was cut off and noise was smoothed out in order to give transparency to the presented results.

## 2.4. The Surface Roughness

The surface roughness of each sample was measured on seven segments, each 6 mm in length, using a 3D profilometer made by Dektak XT (Bruker, Karlsruhe, Germany).

## 2.5. Potentiodynamic Polarization and Electrochemical Impedance Spectroscopy (EIS) Studies

DC electrochemical measurements were performed using specimens with 1 cm<sup>2</sup> of the working area exposed to 3.5% NaCl at room temperature (25 °C). An Atlas Sollich 1131 electrochemical potentiostat (Atlas Sollich, Rebiechowo, Poland) connected to a three-electrode cell was used. The working electrode (WE) was aluminum 5754, whereas the counter (CE) and reference electrodes (SCE) were a platinum and saturated calomel electrode, respectively. The calomel electrode was fixed at about 1 mm away from the surface of the specimen to be tested, and its potential has the value of  $E_{\text{rev}} = 244$  mV relative to the standard hydrogen electrode. The open circuit potential (OCP) was recorded for 30–60 min to achieve changes smaller than 1 mV/min. Tafel curves were obtained by changing the electrode

potential versus the open circuit potential with a scan rate of 1 mV/s. The polarization resistance was calculated using the Stern-Geary equation.

$$R_p = \frac{\beta_a \cdot \beta_c}{2.303(\beta_a + \beta_c) \cdot i_{\text{corr}}}, \quad (2)$$

where  $\beta_a$  and  $\beta_c$  are the anodic and cathodic Tafel slopes, respectively, and  $i_{\text{corr}}$  is the corrosion current density.

Electrochemical Impedance Spectroscopy EIS were carried out at the open circuit potential (OCP) using an ATLAS 1131 Impedance Analyzer. The impedance spectra were acquired in the frequency range of 10 mHz to 100 kHz with a 10-mV amplitude sine wave generated by a frequency response analyzer. Nyquist and Bode plots were obtained after the specimens were immersed in a test solution for 1 h. Generally, three frequency regions, referring to the high, intermediate, and low frequency values, were obtained from impedance spectra. All EIS measurements were conducted at room temperature (25 °C).

### 3. Results and Discussion

Selected microscope images of the 5754 aluminum alloy are shown in Figure 1.

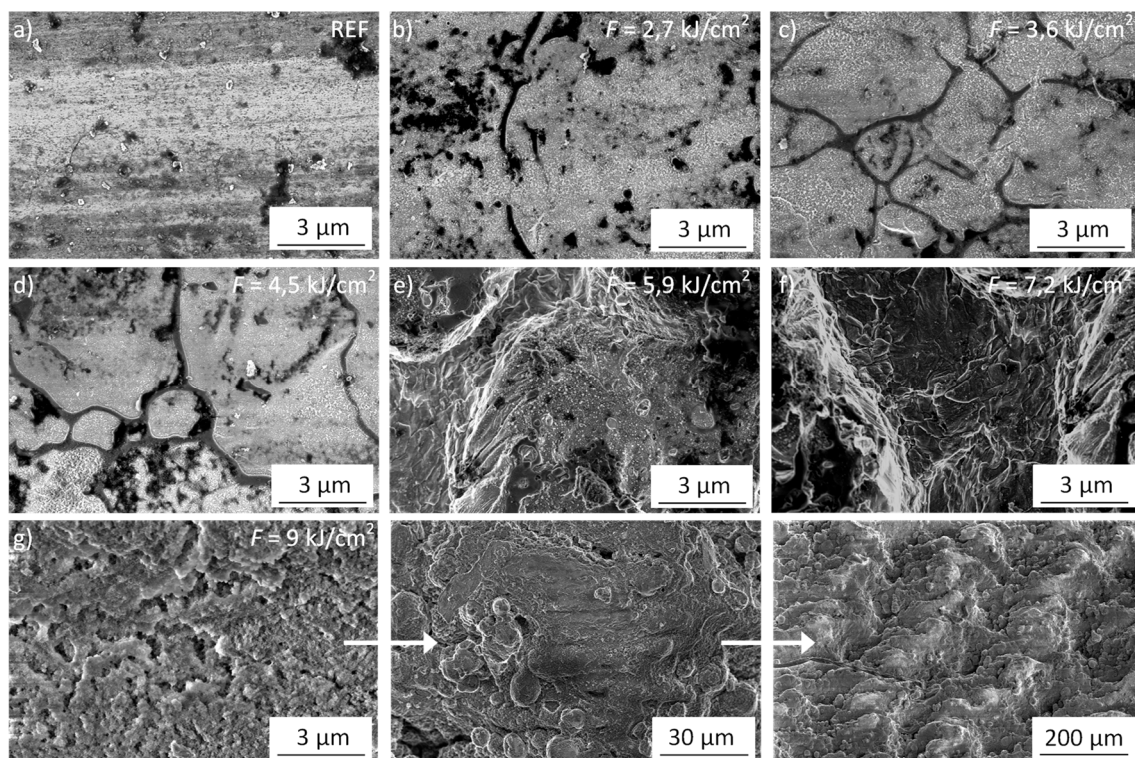


**Figure 1.** Microscopic images of the surface of aluminium 5754, (a) reference sample and after laser irradiation with the laser fluence, (b) 2.7, (c) 3.6, (d) 4.5, (e) 5.9, (f) 7.2, and (g) 9 kJ/cm<sup>2</sup>. To better visualize the roughness, additional magnifications are added for the fluence of 9 kJ/cm<sup>2</sup>.

On the reference sample (Figure 1a), surface heterogeneities (inclusions, defects) are visible. Laser modification contributed to a marked change in the surface morphology of all samples. Microscopic images suggest that, for low laser energy densities,  $F < 4.5$  kJ/cm<sup>2</sup>. As a result of the annealing process, an oxide layer forms on the surface (Figure 1b–d). On the other hand, high values of the laser fluence, as a result of high temperature gradients cause ablation and re-melting of the material. This occurs from  $F \sim 5.9$  kJ/cm<sup>2</sup> (Figure 1e–g). In particular, the highest applied laser

fluence  $F = 9 \text{ kJ/cm}^2$ , causes a significant modification in the geometric structure (surface roughness) (Figure 1g). Heterogeneities and surface defects are conducive to the appearance of corrosion [11].

In order to accurately assess the surface of the sample, a roughness measurement was carried out (Figure 2). Two parameters were used for this purpose:  $R_a$ —the mean roughness profile and  $R_z$ —the largest profile height (the sum of the highest rise of the profile and the depth of its lowest valley within the roughness sampling length). As a result of laser treatment with  $F < 4.5 \text{ kJ/cm}^2$ , compared to the reference sample, the smoothing of the surface is observed. Then, with increasing laser energy density, an increase in roughness is obtained. It is also in line with the research of Zhang et al. [13]. The highest roughness was obtained for a sample irradiated with  $F = 9 \text{ kJ/cm}^2$ , which is in line with the microscopic observations (Figure 1). It is mainly due to the point interaction of the laser beam with the material as well as rapid heating and cooling of its surface. A wavy-like topography was also observed after the KrF excimer [8,9] and fiber laser treatment [13].

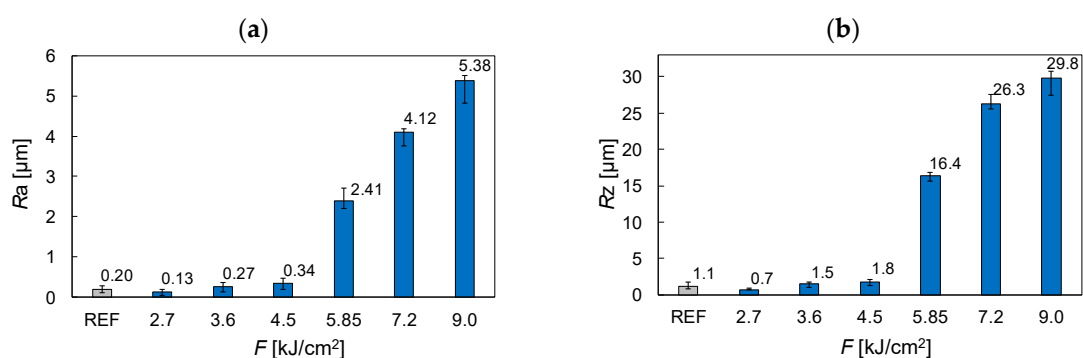


**Figure 2.** The average values of roughness parameters for the reference and laser-irradiated samples, including (a) the mean roughness  $R_a$  and (b) the largest profile height  $R_z$ .

Selected potential-time curves of aluminum 5754 are shown in Figure 3a. As can be seen, the potential becomes more and more noble, while the alloy becomes passivated. The exception is the sample irradiated with the laser fluence of  $F = 9 \text{ kJ/cm}^2$ , in which active dissolution seems to be observed. Figure 3b presents the selected potentiodynamic curves of the 5754 aluminum alloy for different laser energy density. All the surfaces display different corrosion potentials. The electrochemical measurements have shown that, depending on the laser fluence, an improvement ( $F \leq 4.5 \text{ kJ/cm}^2$ ) or deterioration ( $F > 4.5 \text{ kJ/cm}^2$ ) in corrosion resistance of the 5754 aluminum alloy can be obtained. The obtained results coincide with roughness tests (Figure 2).

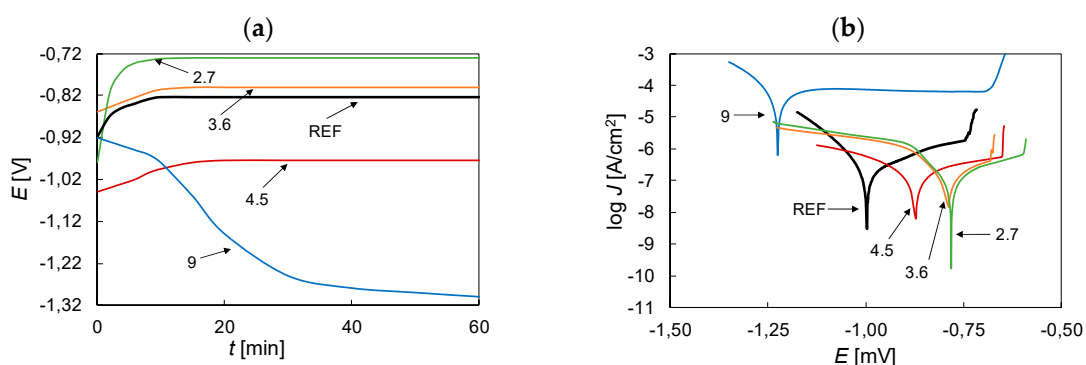


**Figure 3.** Electrochemical measurement of 5754 aluminum alloy taken in the 3% NaCl solution: (a) the potential-time curve and (b) selected potentiodynamic curves.

The polarization resistance  $R$ , corrosion current density  $J$ , and corrosion potential  $E$  (Figure 4), were determined using the Tafel method. Each sample was measured five times. In electrochemical

measurements, the corrosion current density  $J$  indicates the intensity of the process. The lower the value, the slower the corrosion process. In other words, the sample is more resistant. The corrosion potential  $E$  indicates a susceptibility to corrosion. The higher (less negative) the corrosion, the better. The polarization resistance  $R$  determines the corrosion resistance. The higher the value, the more corrosion resistant the sample is. For the sample irradiated with higher laser fluence ( $F > 4.5 \text{ kJ/cm}^2$ ), a decrease in polarization resistance  $R$  and corrosion potential  $E$ , as well as a significant increase in the corrosion current density  $J$  are observed, which suggests a significant decrease in the corrosion resistance (compared to the reference sample). It is mainly evident from the high temperature gradients and material ablation (the surface of the aluminum is modified with both its chemical and geometrical structure) during the laser process. High roughness and numerous heterogeneities (Figures 1 and 2) result in a decrease in corrosion resistance. Completely different corrosion behavior is observed for the samples irradiated with lower laser energy density ( $F \leq 4.5 \text{ kJ/cm}^2$ ). This is an increase in corrosion resistance compared to the reference sample. For low values of the laser energy density, it seems that a thin passive layer is formed on the surface of the material. The decrease of corrosion current density after laser surface treatment was also observed in the research by Embuka et al. [9] and Zhang et al. [13], respectively.

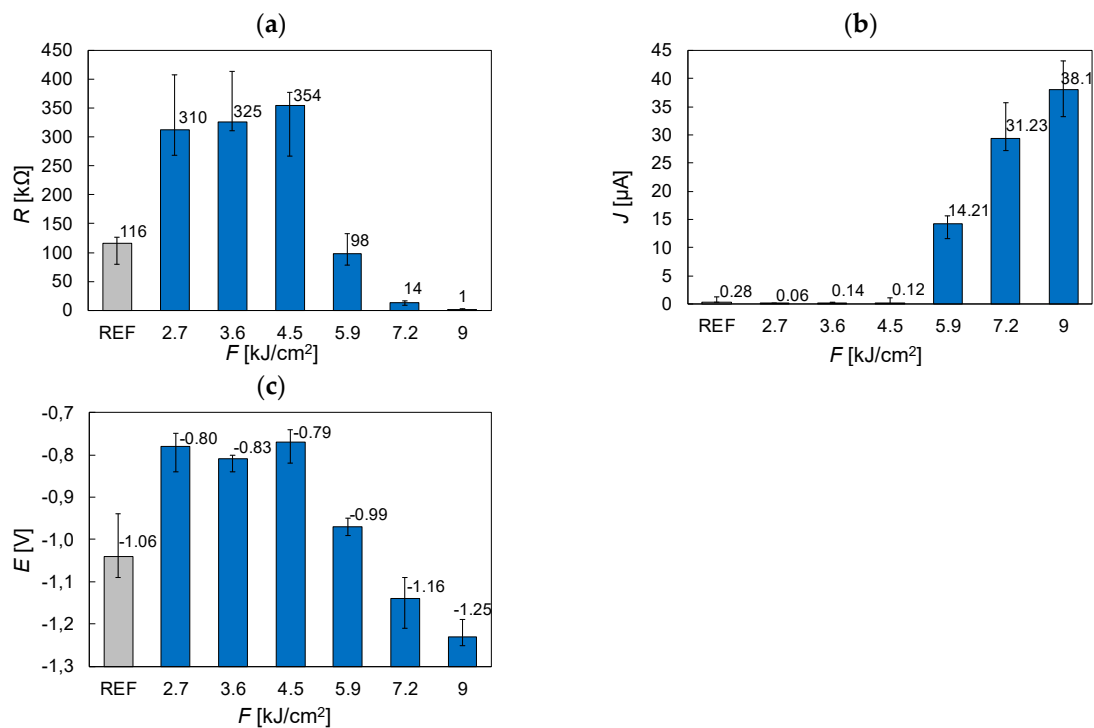


**Figure 4.** Electrochemical measurements: (a) the polarization resistance  $R$ , (b) corrosion current density  $J$ , and (c) potential  $E$  as a function of laser energy density ( $V = 10 \text{ mm/s}$ ,  $h = 10 \text{ μm}$ ,  $PRR = 80 \text{ kHz}$ ), taken in a 3.5% NaCl environment. The results are the average of five measurements.

Electrochemical impedance spectroscopy confirmed the results of potentiodynamic tests (Figure 4). Spectra of Bode and Nyquist are summarized in Figure 5. The highest values of the impedance module  $|Z|$ , in the whole frequency range, were obtained for samples exposed to low fluence values of 2.7 and 3.6 kJ/cm<sup>2</sup>, which suggests their highest corrosion resistance in the tested environment (Figure 5a). For these samples, the phase angle  $\varphi$  also reached its highest values and was close to 90° in a wide frequency range (Figure 5b). As expected, the sample was irradiated with the highest energy density  $F = 9 \text{ kJ/cm}^2$  showed the lowest corrosion resistance in a 3.5% NaCl solution. In the Nyquist spectra (Figure 5c,d), the purely capacitive nature of the irradiated sample with the lowest fluence (2.7 kJ/cm<sup>2</sup>) was observed. In this case, the process was mainly controlled by diffusion. Semi-circles appeared

in the Nyquist spectra for higher fluences and the reference sample. The larger the semi-circle, the lower the corrosion rate is. The shape of induction loops (semi-circle) also suggests instability of the system during measurements due to the initiation of corrosion. The smallest diameter of the semi-circle was obtained for the sample exposed to the highest laser energy density (fluence), which confirms its weakest corrosion properties.

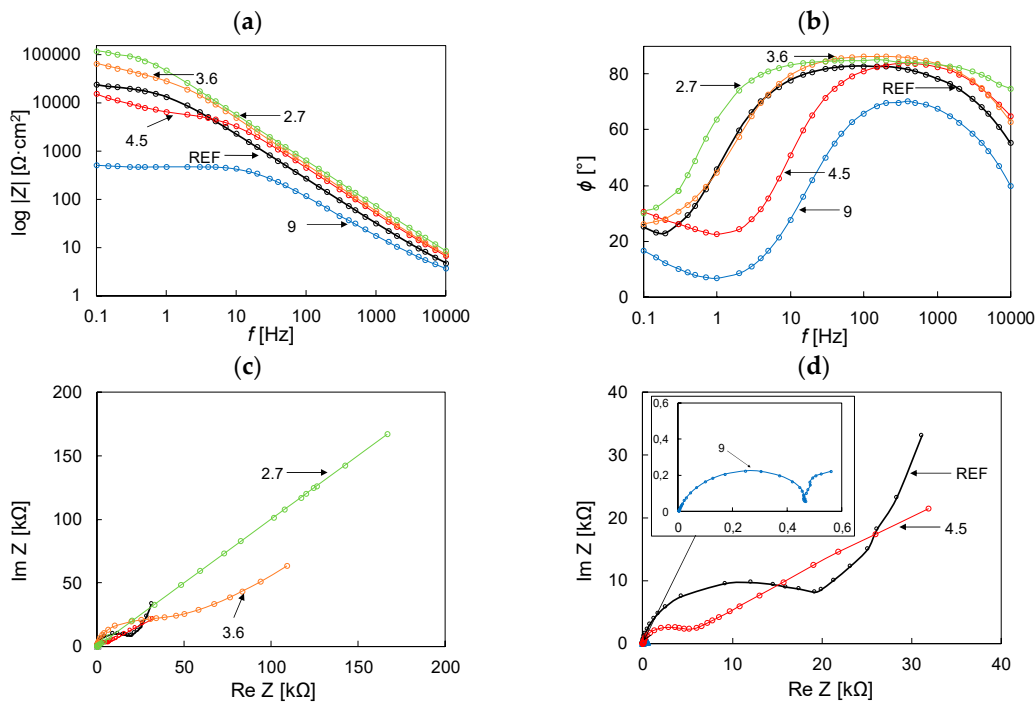


**Figure 5.** Electrochemical Impedance Spectroscopy EIS data obtained in 3.5% NaCl solution for the reference and laser-treated samples, including (a) Bode plots-impedance, (b) Bode plots-phase angle, and (c) Nyquist plots (d) enlarging the Nyquist plot fragment.

The obtained spectra (Figure 5) were fitted to the equivalent circuit (Figure 6a,b) using AtlasLab version 2.24 software, which is dedicated to electrochemical measurements. The electrical circuit was comprised of three resistors and two capacitors.  $R_s$  is the solution resistance. The constant phase elements (CPEs) for the representation of the capacitances of different layers were applied. The parameters  $R_1$  and  $CPE_1$  (Figure 6a) are connected with the outer layer, which corresponds to the upper layer of the oxygen-rich region [13]. The  $R_2$  and  $CPE_2$  relate to the oxide layer that corresponds to the lower part of the oxygen-poor region. In Figure 6b,  $R_1$  and  $CPE_1$  correspond to the resistance and capacity of the passive (oxygen-rich) layer.

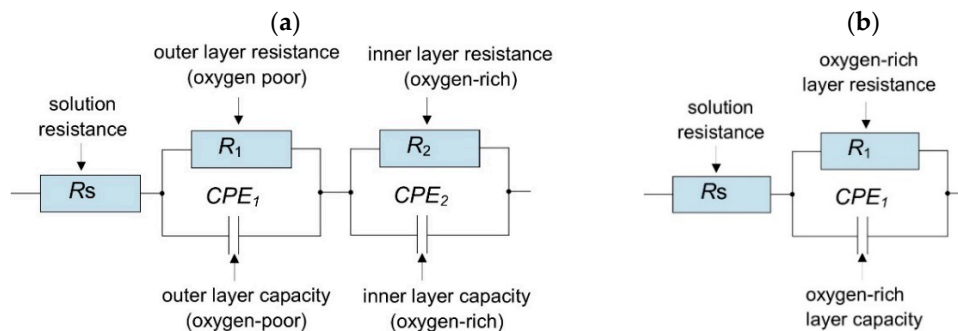


**Figure 6.** Equivalent circuits of the Electrochemical Impedance Spectroscopy EIS spectra: (a) two-layer model, and (b) one-layer model.

The resistance of the outer layer  $R_1$  was lower than the resistance of the oxide layer  $R_2$ , which suggests that the outer layer was less protective. The highest value of the oxide protective layer was obtained for  $F = 2.7 \text{ kJ/cm}^2$ , which suggests the highest corrosion resistance among the tested samples and is in line with previous results. Moreover, for this sample, the appearance of a semicircle or inductive loop was not observed. It seems that the model has only one oxide layer. The fitting results of electrical components are summarized in Table 3.

**Table 3.** Impedance parameters of aluminium 5754 alloy in 3.5% NaCl solution, where:  $R_S$ —solution resistance,  $R_1$ —outer layer resistance,  $Y_1$ —passive layer admittance,  $R_2$ —oxide layer resistance,  $Y_2$ —outer layer admittance,  $N_1, N_2$ —shape factors, \*—results fitted to the model from Figure 6b.

$F \text{ [kJ/cm}^2\text{]}$	$R_S \text{ [}\Omega\text{]}$	$Y_1 \text{ [}\mu\text{S]}$	$N_1$	$R_1 \text{ [}\Omega\text{]}$	$Y_2 \text{ [}\mu\text{S]}$	$N_2$	$R_2 \text{ [k}\Omega\text{]}$
0 (REF)	1.11	178	0.96	1.11	9.92	0.94	18.56
2.7*	1.71	3.56	0.99	125,594	-	-	-
3.6	1.42	57.1	0.99	1.42	4.21	0.97	40.20
4.5	0.79	144	0.98	0.79	4.52	0.99	5.32
9.0	1.17	9610	0.94	1.18	31.65	0.86	0.50

Figure 7 presents the results of chemical tests on EDX. As expected, an increase in the laser fluence caused an increase in the proportion of oxygen in the analyzed layer, mainly at the expense of aluminum (Figure 7a). With the increase of the laser energy density (and, thus, with the increase of oxidation of the layer), the content of other elements also decreased (Figure 7b). The decrease in Cu lowers the overall potential of the Cu-rich phases [10]. Nevertheless, due to the significant depth of penetration during the analysis ( $\sim 2\text{--}3 \mu\text{m}$ ), the obtained result should be treated as the average value of the concentration of individual factors both in the oxide layer, as well as in the subsurface layer of the substrate itself.

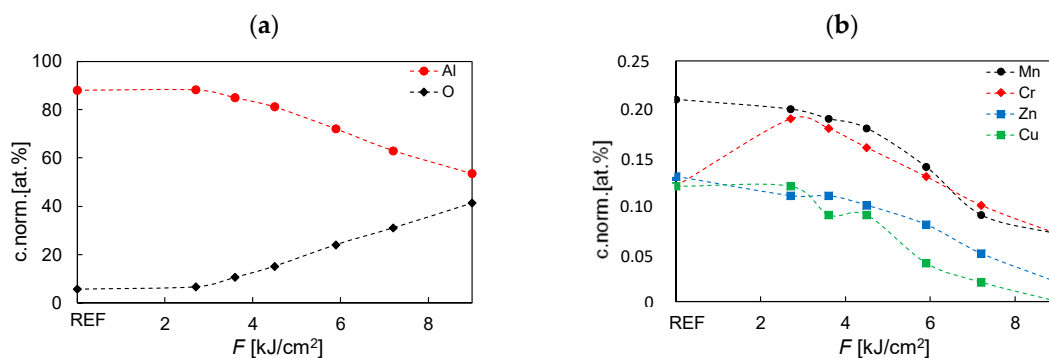


**Figure 7.** Chemical composition (at.%) of created oxide layers as a function of laser power for chosen elements: (a) aluminum and oxide, (b) manganese, chrome, zinc, and copper.

Laser-induced thin oxide layers have a complex physico-chemical structure that changes with the laser energy density. The layers formed by laser annealing are a gradient (they grow from the substrate). There is no clear boundary between the oxide produced and the substrate material. Therefore, chemical composition analysis is difficult. Raman spectra are complex and ambiguous (Figure 8). However, it can be seen that the high-fluence sample has a spectrum more similar to the referential sample than the low-fluency samples (in which improvement of corrosion properties was noted). However, due to the fact that mainly non-stoichiometric compounds are formed, it is difficult to assign individual bands to individual compounds. Some bands are poorly separated due to the close proximity of different signals. Aluminum oxides in the  $\text{Al}_2\text{O}_3$ ,  $\text{AlO}_4$ , and  $\text{AlO}_6$  forms predominate in the spectra. Aluminum oxide forms testify to the presence of a passive layer on the surface of the substrate,

which is characteristic of this type of substrate. The observed wide signals near 1016, 1056, and 1068  $\text{cm}^{-1}$  may come from an Al–O bending mode [15]. For fluency of 3.6  $\text{kJ}/\text{cm}^2$ , a peak appears at 934  $\text{cm}^{-1}$ , which can be derived from symmetric stretch Al–O–Al. Broad signals were detected for all samples, near 809  $\text{cm}^{-1}$  from vibration groups  $\gamma$ -Al(OH)<sub>3</sub> or condensed AlO<sub>4</sub> [16,17]. Around 720  $\text{cm}^{-1}$ , AlO<sub>4</sub> appears to occur. Nearly 640  $\text{cm}^{-1}$  (sample subjected to higher energy density  $F \geq 4.5 \text{ kJ}/\text{cm}^2$ ), there are characteristic signals from amorphous Al<sub>2</sub>O<sub>3</sub> [18]. A peak at 560  $\text{cm}^{-1}$  may be associated with  $\gamma$ -Al<sub>2</sub>O<sub>3</sub> formation. Signals near 468, 487, and 606  $\text{cm}^{-1}$  may come from the AlO<sub>6</sub> insulated form of alumina [18]. Vibration of  $\alpha$ -AlOOH groups has characteristic signals near 315 and 295  $\text{cm}^{-1}$  [16,17]. In the case of samples irradiated with low laser fluence ( $F < 4.5 \text{ kJ}/\text{cm}^2$ ), peaks around 265  $\text{cm}^{-1}$  were observed, which may be due to vibrations of the tetrahedral or octahedral form of alumina (AlO<sub>4</sub> or AlO<sub>6</sub>) [18].

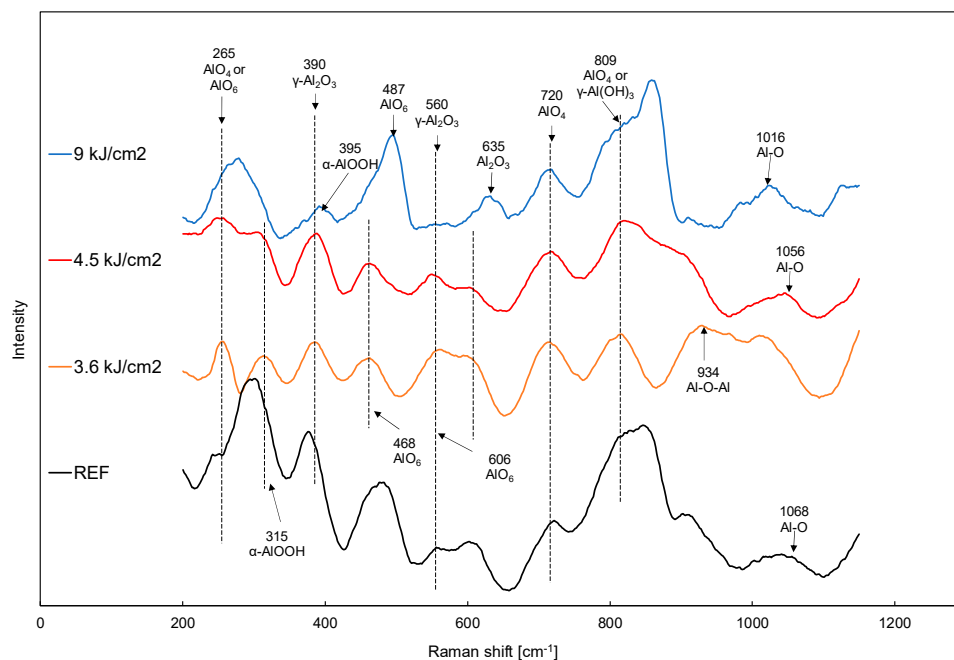


Figure 8. Raman spectra for reference and laser-treated aluminum 5754.

#### 4. Conclusions

In this paper, the corrosion behavior of 5754 aluminum alloy in 3.5% NaCl environment, after irradiation using a laser with a long pulse duration  $\tau = 230 \text{ ns}$ , was analyzed. The processes in a direct laser writing mode do not allow the creation of the homogeneous coating. Regarding a significantly large ablation threshold ( $F = 9 \text{ kJ}/\text{cm}^2$ ), due to high temperature gradients causing numerous heterogeneities, and significantly increasing the roughness, the corrosion resistance decreases. Nevertheless, using low values of the laser energy density (below the ablation threshold), allows the improvement of the corrosion resistance due to the simultaneous oxide layer creation. Laser-induced thin oxide layers have a complex physico-chemical structure that changes with the laser energy density. The chemical analysis has shown that the surface of the material is oxidized. Oxide forms formed on the surface testifies of the presence of a passive layer on substrate surfaces.

**Author Contributions:** Conceptualization, K.M.M.; methodology, K.M.M.; data curation: K.M.M. and J.G.; writing—original draft preparation, K.M.M.; writing—review and editing, K.M.M. and A.J.A.; visualization, K.M.M.; supervision, A.J.A.

**Funding:** The research was supported by statutory funds No. 0401/0031/18.

**Conflicts of Interest:** The authors declare no conflict of interest.

## References

1. Sherif, E.S.M. Corrosion and Corrosion Inhibition of Aluminum in Arabian Gulf Seawater and Sodium Chloride Solutions by 3-Amino-5-Mercapto-1,2,4-Triazole. *Int. J. Electrochem. Sci.* **2011**, *6*, 1479–1492.
2. Kliškić, M.; Radošević, J.; Gudić, S.; Katalinić, V. Aqueous extract of *Rosmarinus officinalis* L. as inhibitor of Al-Mg alloy corrosion in chloride solution. *J. Appl. Electrochem.* **2000**, *30*, 823–830. [[CrossRef](#)]
3. Vargel, C. *Corrosion of Aluminum*; Elsevier: Amsterdam, The Netherlands, 2004.
4. Rehim, S.S.A.; Hassan, H.H.; Amin, M.A. Chronoamperometric studies of pitting corrosion of Al and (Al-Si) alloys by halide ions in neutral sulphate solutions. *Corros. Sci.* **2004**, *46*, 1921–1938. [[CrossRef](#)]
5. Foley, R.T.; Nguyen, T.H. The chemical nature of aluminum corrosion V. Energy transfer in aluminum dissolution. *J. Electrochem. Soc.* **1955**, *11*, 477–486.
6. Bala, H. Korozja materiałów-teoria i praktyka. In *Politechniki Częstochowskiej*; Wydawnictwo WIPMiFS PC: Częstochowa, Poland, 2002.
7. Féron, D. *Corrosion Behaviour and Protection of Copper and Aluminum Alloys in Seawater*; Elsevier: Amsterdam, The Netherlands, 2007; Volume 50.
8. Chan, C.P.; Yue, T.M.; Man, H.C. The effect of excimer laser surface treatment on the pitting corrosion fatigue behaviour of aluminum alloy 7075. *J. Mater. Sci.* **2003**, *38*, 2689–2702. [[CrossRef](#)]
9. Embuka, D.; Coy, A.E.; Hernandez-Barrios, C.A.; Viejo, F.; Liu, Z. Thermal stability of excimer laser melted films formed on the AA2024-T351 aluminium alloy: Microstructure and corrosion performance. *Surf. Coat. Technol.* **2017**, *313*, 214–221. [[CrossRef](#)]
10. Watkins, K.G.; Liu, Z.; McMahon, M.; Vilar, R.; Ferreira, M.G.S. Influence of the overlapped area on the corrosion behaviour of laser treated aluminum alloys. *Mater. Sci. Eng. A* **1998**, *252*, 292–300. [[CrossRef](#)]
11. Bonora, P.L.; Bassoli, M.; De Anna, P.L.; Battaglin, G.; Della Mea, G.; Mazzoldi, P.; Miotello, A. Electrochemical and corrosion behaviour of laser-modified aluminum surfaces. *Electrochim. Acta* **1980**, *73*, 200.
12. Ahuir-Torres, J.I.; Arenas, M.A.; Perrie, W.; Dearden, G.; de Damborenea, J. Surface texturing of aluminium alloy AA2024-T3 by picosecond laser: Effect on wettability and corrosion properties. *Surf. Coat. Technol.* **2017**, *321*, 279–291. [[CrossRef](#)]
13. Zhang, F.D.; Liu, H.; Suebka, C.; Liu, Y.X.; Liu, Z.; Guo, W.; Cheng, Y.M.; Zhang, S.L.; Li, L. Corrosion behavior of laser-cleaned AA7024 aluminum alloy. *Appl. Surf. Sci.* **2018**, *435*, 452–461. [[CrossRef](#)]
14. Antończak, A.J.; Stepak, B.; Koziol, P.; Abramski, K. The influence of process parameters on the laser-induced coloring of titanium. *Appl. Phys. A* **2014**, *115*, 1003–1013. [[CrossRef](#)]
15. Cherepy, N.J.; Shen, T.H.; Esposito, A.P.; Tillotson, T.M. Characterization of an effective cleaning procedure for aluminum alloys: Surface enhanced Raman spectroscopy and zeta potential analysis. *J. Colloid Interface Sci.* **2005**, *282*, 80–86. [[CrossRef](#)] [[PubMed](#)]
16. Jinlong, L.; Hongyun, L.; Jinpeng, X. Experimental study of corrosion behavior for burnished aluminum alloy by EWF, EBSD, EIS and Raman spectra. *Appl. Surf. Sci.* **2013**, *273*, 192–198. [[CrossRef](#)]
17. Lekatou, A.; Sfikas, A.K.; Karantzalis, A.E.; Sioulas, D. Microstructure and corrosion performance of Al-32% Co alloys. *Corros. Sci.* **2012**, *63*, 193–209. [[CrossRef](#)]
18. Thomas, P.V.; Ramakrishnan, V.; Vaidyan, V.K. Oxidation studies of aluminum thin films by Raman spectroscopy. *Thin Solid Films* **1989**, *170*, 35–40. [[CrossRef](#)]

